

Effects of chiral three-nucleon forces on ^4He -nucleus scattering in a wide range of incident energies

Masakazu Toyokawa,^{1,*} Masanobu Yahiro,¹ Takuma Matsumoto,¹ and Michio Kohno²

¹*Department of Physics, Kyushu University, Fukuoka 819-0395, Japan*

²*Research Center for Nuclear Physics (RCNP), Osaka University, Ibaraki 567-0047, Japan*

(Dated: December 27, 2017)

Background: It is a current important subject to clarify properties of chiral three-nucleon forces (3NFs) not only in nuclear matter but also in scattering between finite-size nuclei. Particularly for the elastic scattering, this study has just started and the properties are not understood in a wide range of incident energies (E_{in}).

Aims and approach: We investigate basic properties of chiral 3NFs in nuclear matter with positive energies by using the Brueckner-Hartree-Fock method with chiral two-nucleon forces at N^3LO and 3NFs at NNLO , and analyze effects of chiral 3NFs on ^4He elastic scattering from targets ^{208}Pb , ^{58}Ni and ^{40}Ca over a wide range of $30 \lesssim E_{\text{in}}/A_{\text{P}} \lesssim 200$ MeV by using the g -matrix folding model, where A_{P} is the mass number of the projectile.

Results: In symmetric nuclear matter with positive energies, chiral 3NFs make the single-particle potential less attractive and more absorptive. The effects mainly come from the Fujita-Miyazawa 2π -exchange 3NF and slightly become larger as E_{in} increases. These effects persist in the optical potentials of ^4He scattering. As for the differential cross sections of ^4He scattering, chiral-3NF effects are large in $E_{\text{in}}/A_{\text{P}} \gtrsim 60$ MeV and improve the agreement of the theoretical results with the measured ones. Particularly in $E_{\text{in}}/A_{\text{P}} \gtrsim 100$ MeV, the folding model reproduces measured differential cross sections pretty well. Cutoff (Λ) dependence is investigated for both nuclear matter and ^4He scattering by considering two cases of $\Lambda = 450$ and 550 MeV. The uncertainty coming from the dependence is smaller than chiral-3NF effects even at $E_{\text{in}}/A_{\text{P}} = 175$ MeV.

PACS numbers: 21.30.Fe, 24.10.Ht, 25.55.Ci

I. INTRODUCTION

How do three-nucleon forces (3NFs) work in nuclear many-body systems? This is an important subject to be answered in nuclear physics. Even if 3NFs do not exist on a fundamental level, they come out in effective theories with a finite momentum cutoff Λ by renormalizing the degrees of freedom present above Λ . The representative example is the 2π -exchange process with intermediate nucleon excited states, typically the $\Delta(1232)$ isobar. It is now called the Fujita-Miyazawa 3NF [1]. As a phenomenological approach, attractive 3NFs were introduced to reproduce the binding energies for light nuclei [2], whereas repulsive 3NFs were used to explain the empirical saturation properties in symmetric nuclear matter [3].

Essential progress on this subject was made by chiral effective field theory (EFT) [4, 5] based on chiral perturbation theory. The theory provides a low-momentum expansion of two-nucleon force (2NF), 3NF and many-nucleon forces, and makes it possible to define the forces systematically. Figure 1 shows chiral 3NFs in the next-to-next-to-leading order (NNLO). Diagram (a) corresponds to the Fujita-Miyazawa 2π -exchange 3NF [1], and diagrams (b) and (c) mean 1π -exchange and con-

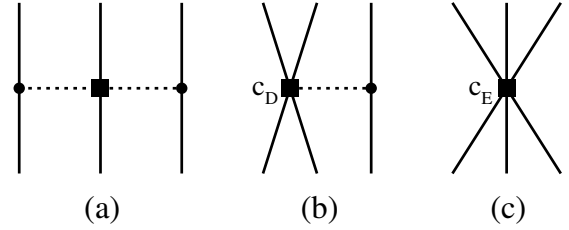


FIG. 1: 3NFs in NNLO. Diagram (a) corresponds to the Fujita-Miyazawa 2π -exchange 3NF [1], and diagrams (b) and (c) correspond to 1π -exchange and contact 3NFs. The solid and dashed lines denote nucleon and pion propagations, respectively, and filled circles and squares stand for vertices. The strength of the filled-square vertex is often called c_D in diagram (b) and c_E in diagram (c).

tact 3NFs, respectively. The filled-square vertex has a strength c_D in the diagram (b) and c_E in the diagram (c). Quantitative roles of chiral 3NFs were extensively investigated, particularly for light nuclei and nuclear matter [6]; more precisely, see Ref. [7] for light nuclei, Refs. [8, 9] for *ab initio* nuclear-structure calculations in lighter nuclei and Refs. [10–16] for nuclear matter. In addition, effects of chiral four-nucleon forces were found to be small in nuclear matter [17, 18]. The chiral g matrix, calculated from chiral 2NF+3NF with the Brueckner-Hartree-Fock (BHF) method, yields a reasonable nuclear matter sat-

*toyokawa@phys.kyushu-u.ac.jp

uration curve for symmetric nuclear matter, when the parameters, c_D and c_E , of NNLO 3NFs are tuned [13].

Nuclear scattering is another place to investigate 3NF effects. The theoretical description of $N+d$ scattering has been naturally associated with the necessity of 3NFs [7, 19], when the theory starts with sophisticated 2NFs determined from the experiments. Microscopic evaluation of nuclear optical potentials for nucleon-nucleus (NA) and nucleus-nucleus (AA) elastic scattering has a long history. The g -matrix folding model [20–25] is a standard method for deriving the optical potentials of NA and AA elastic scattering microscopically. In fact, the potentials have been used to analyze various kinds of nuclear reactions in many papers. In the model, the optical potentials were obtained by folding the g matrix [20–25] with the projectile (P) density ρ_P and the target (T) one ρ_T . This description has been quite successful in explaining many elastic scattering. At first, the effects of 3NFs were phenomenologically investigated in Ref. [23] for NA elastic scattering and in Refs. [22, 26] for NA and AA elastic scattering. The 3NFs reduce differential cross section and improve the agreement with measured vector analyzing powers. However, the role of 3NFs has not been clarified quantitatively, because the folding potential is adjusted to measured cross sections.

In Refs. [27, 28], as the first attempt, we made qualitative discussion for chiral-3NF effects on elastic scattering by using the hybrid method in which the existing local version of Melbourne g matrix [21] was modified on the basis of the chiral g matrix constructed from chiral 2NFs and 3NFs. The work showed that chiral-3NF effects are small for NA elastic scattering, but important for AA elastic scattering. Recently, we directly parameterized the chiral g matrix as a local potential based on chiral 2NF+3NF, as briefly reported in Ref. [25]. In this paper, we present a full understanding of chiral-3NF effects on ^4He elastic scattering over a wide range of $30 \lesssim E_{\text{in}}/A_P \lesssim 200$ MeV by using the local version of the chiral g matrix, where E_{in} stands for an incident energy in the laboratory system and A_P is the mass number of projectile.

The g matrices calculated so far are provided by a local potential with Yukawa or Gaussian form, since this procedure makes the folding calculation much easier.

Investigation of chiral-3NF effects on NA and AA elastic scattering has just started with lower incident energies per nucleon such as $E_{\text{in}}/A_P \approx 70$ MeV by using the g -matrix folding model [25, 27, 28], since chiral EFT is more reliable for lower incident energies. As mentioned above, the folding potentials were recently calculated from the local version of chiral g matrix in Ref. [25]. The chiral g -matrix folding model accounts for experimental data considerably well on NA scattering at $E_{\text{in}} = 65$ MeV and $^4\text{He}+^{58}\text{Ni}$ scattering at $E_{\text{in}}/A_P = 72$ MeV. This model also showed that chiral-3NF effects are small for NA elastic scattering, but sizable for ^4He elastic scattering.

In our previous studies for ^4He elastic scattering, we used the Melbourne g matrix in Ref. [29] and the chiral

g matrices based on chiral 2NF and chiral 2NF+3NF in Ref. [25]. After Ref. [25] was published, we found some numerical errors in our nuclear-matter calculations including chiral 3NFs; see Ref. [30] for the details. In the present work, we then adopt the corrected version of chiral g -matrix; see Appendix for the matrix. Further discussion will be made later in Sec. II B.

In this paper, we first investigate basic properties of chiral 3NFs in symmetric nuclear matter for *positive energies* up to 200 MeV by using the BHF method with chiral 2NFs of N^3LO and chiral 3NFs of NNLO. We show that chiral-3NF effects provide density-dependent repulsive and absorptive corrections to the single-particle potential and that the effects slightly become larger as the energy increases. We also point out that the corrections mainly come from the Fujita-Miyazawa 2π -exchange 3NF of diagram (a).

Second, we analyze chiral-3NF effects on ^4He scattering from various targets in a *wide range of incident energies* by using the chiral g -matrix folding model. In order to make our discussion clear, we take ^4He scattering as AA scattering, since the g -matrix folding model is confirmed to work well for ^4He scattering in virtue of negligibly small projectile-breakup effects [29, 31]; see Sec. IID for further discussion. In addition, as targets we take heavier nuclei, ^{208}Pb , ^{58}Ni and ^{40}Ca , since the g matrix is evaluated in nuclear matter and is considered to be more suitable for heavier targets. For the targets, the experimental data are available in a wide range of $30 \lesssim E_{\text{in}}/A_P \lesssim 200$ MeV.

In the present paper, we mostly consider the case of the cutoff scale $\Lambda = 550$ MeV. As the third subject, Λ dependence is investigated for nuclear matter with positive energies and ^4He elastic scattering by taking two other cases of $\Lambda = 450$ and 550 MeV.

Finally, we provide the local version of chiral g matrix including chiral-3NF effects with a 3-range Gaussian form for the case of $E_{\text{in}}/A_P = 75$ MeV. This may strongly encourage the application of the chiral g matrix for studying various kinds of nuclear reactions. This local version of chiral g matrix is referred to as “Kyushu chiral g matrix” in this paper.

In Sec. II, we present the theoretical framework composed of the BHF method and the folding model, and show some basic results of BHF calculations for chiral 2NF+3NF. In Sec. III, the results of the chiral g -matrix folding model are shown for ^4He elastic scattering. Section IV is devoted to a summary.

II. THEORETICAL FRAMEWORK AND BASIC RESULTS

A. BHF equation for 2NF+3NF

We first recapitulate the BHF method for 2NF+3NF, following Ref. [12]. Because it is not easy to treat a 3NF V_{123} even in nuclear matter, we introduce an effective

2NF V_{12}^{eff} by applying the mean-field approximation, or the normal ordering prescription, to the 3NF:

$$\begin{aligned} & \frac{1}{2} \sum_{\mathbf{k}_1 \mathbf{k}_2} \langle \mathbf{k}_1 \mathbf{k}_2 | V_{12} | \mathbf{k}_1 \mathbf{k}_2 \rangle_{\mathcal{A}} \\ & + \frac{1}{3!} \sum_{\mathbf{k}_1 \mathbf{k}_2 \mathbf{k}_3} \langle \mathbf{k}_1 \mathbf{k}_2 \mathbf{k}_3 | V_{123} | \mathbf{k}_1 \mathbf{k}_2 \mathbf{k}_3 \rangle_{\mathcal{A}} \\ & = \frac{1}{2} \sum_{\mathbf{k}_1 \mathbf{k}_2} \langle \mathbf{k}_1 \mathbf{k}_2 | V_{12}^{\text{eff}} | \mathbf{k}_1 \mathbf{k}_2 \rangle_{\mathcal{A}}, \end{aligned} \quad (1)$$

where \mathcal{A} means the antisymmetrization and \mathbf{k}_i corresponds to quantum numbers of the i -th nucleon. Equation (1) leads

$$V_{12}^{\text{eff}} = V_{12} + \frac{1}{3} V_{12(3)}, \quad (2)$$

where $V_{12(3)}$ is defined by summing up 3NF V_{123} over the third nucleon in the Fermi sea:

$$\langle \mathbf{k}'_1 \mathbf{k}'_2 | V_{12(3)} | \mathbf{k}_1 \mathbf{k}_2 \rangle_{\mathcal{A}} = \sum_{\mathbf{k}_3} \langle \mathbf{k}'_1 \mathbf{k}'_2 \mathbf{k}_3 | V_{123} | \mathbf{k}_1 \mathbf{k}_2 \mathbf{k}_3 \rangle_{\mathcal{A}} \quad (3)$$

with assuming the center-of-mass (c.m.) frame: $\mathbf{k}'_1 + \mathbf{k}'_2 = \mathbf{k}_1 + \mathbf{k}_2$. Note the factor $1/3$ in Eq. (2). The g matrix g_{12} is a solution to the BHF equation

$$g_{12} = V_{12}^{\text{eff}} + V_{12}^{\text{eff}} G_0 g_{12}, \quad (4)$$

where G_0 is the nucleon propagator with the Pauli exclusion operator in the numerator and with the single-particle energy

$$e_{\mathbf{k}} = \langle \mathbf{k} | T | \mathbf{k} \rangle + \text{Re}[\mathcal{U}(\mathbf{k})] \quad (5)$$

of the nucleon having a momentum \mathbf{k} in the denominator. Here T is the standard kinetic-energy operator of nucleon, and the single-particle potential $\mathcal{U}(\mathbf{k})$ is defined by [12]

$$\mathcal{U}(\mathbf{k}) = \sum_{|\mathbf{k}'| \leq k_F} \langle \mathbf{k} \mathbf{k}' | \tilde{g}_{12} | \mathbf{k} \mathbf{k}' \rangle_{\mathcal{A}}. \quad (6)$$

with the effective g matrix, so-called \tilde{g} matrix, including additional rearrangement terms of the 3NF origin:

$$\tilde{g}_{12} = g_{12} + \frac{1}{6} V_{12(3)} (1 + G_0 g_{12}). \quad (7)$$

Note that \mathbf{k} is related to the incident energy E_{in} as $E_{\text{in}} = (\hbar \mathbf{k})^2 / (2m) + \text{Re}[\mathcal{U}]$. The present formulation is consistent with the second-order perturbation of Ref. [32], because of the factor $1/6$ in Eq. (7). For the symmetric nuclear matter where the proton density ρ_p agrees with the neutron one ρ_n , the Fermi momentum k_F is related to the matter density $\rho = \rho_p + \rho_n$ as $k_F^3 = 3\pi^2 \rho / 2$, so that the normal density $\rho = \rho_0 = 0.17 \text{ fm}^{-3}$ is realized at $k_F = 1.35 \text{ fm}^{-1}$.

B. Some basic results of BHF calculations

The \tilde{g} matrix is calculated from chiral 2NF of N^3LO and chiral 3NF of NNLO by using the BHF method. In BHF calculations, the form factor $\exp\{-(q'/\Lambda)^6 - (q/\Lambda)^6\}$ is introduced for both V_{12} and $V_{12(3)}$. We mainly consider the case of $\Lambda = 550 \text{ MeV}$, and take another case $\Lambda = 450 \text{ MeV}$ when Λ dependence of physical quantities is estimated. The low-energy constants relevant for 3NFs are $(c_1, c_3, c_4) = (-0.81, -3.4, 3.4)$ [33] in units of GeV^{-1} .

As noted earlier, some errors were found in nuclear-matter calculations with chiral 3NFs of Ref. [12], after Ref. [25] was published. Although the qualitative importance of chiral 3NFs for improving nuclear matter saturation properties does not change, the saturation curve is changed by the corrections. To restore reasonable nuclear saturation properties, which are basically important for further application for microscopic derivation of nuclear optical potentials, the remaining two parameters c_D and c_E are tuned [30]. In consideration of the uncertainty that the c_D and c_E terms yield almost identical contributions when $c_D \simeq 4c_E$, c_D is determined as -2.5 by setting $c_E = 0$ for $\Lambda = 450 \text{ MeV}$ and next c_E is fixed as 0.25 for $\Lambda = 550 \text{ MeV}$ with keeping $c_D = -2.5$. These values are somewhat different from those determined in few-body systems within continuous uncertainties. It has been recognized [9], however, that low-energy-constants fixed solely in few-body systems are not adequate in heavier systems. In this article, we use the corrected version of the chiral g matrix.

It is known that chiral 3NFs make repulsive corrections to the binding energy of symmetric nuclear matter [12]. What happens in positive energy? Figure 2 shows E_{in} dependence of \mathcal{U} for the case of $k_F = 1.2 \text{ fm}^{-1}$ for the cutoff $\Lambda = 550 \text{ MeV}$. This density is realized in the peripheral region of a target nucleus and hence important for elastic scattering. Filled (open) circles denote the results of BHF calculations with (without) chiral 3NFs. One can see that chiral 3NFs make \mathcal{U} less attractive and more absorptive. The 3NF corrections slightly increase as E_{in} goes up. Our results are consistent with the second-order perturbation calculation by Holt *et al.* [32].

Figure 3 shows \mathcal{U} as a function of E_{in} at $k_F = 1.2 \text{ fm}^{-1}$, but two cases of $\Lambda = 450$ and 550 MeV are taken in BHF calculations to see the uncertainty coming from Λ dependence on \mathcal{U} . The Λ dependence is plotted as an error bar. The error bar plotted by a solid (dashed) line denotes the results of BHF calculations with (without) chiral 3NFs; note that panels (a) and (b) correspond to the real and imaginary parts of \mathcal{U} . Particularly for BHF calculations with chiral 3NFs, there is a tendency that the uncertainty become larger as E_{in} increases from 80 MeV . Even at $E_{\text{in}} = 175 \text{ MeV}$, however, chiral 3NF effects are larger than the uncertainty. This enables us to make reliable discussion on chiral-3NF effects.

In order to obtain deeper understanding of the properties of chiral 3NFs, we classify $\tilde{g}(k_F, E_{\text{in}})$ with the total

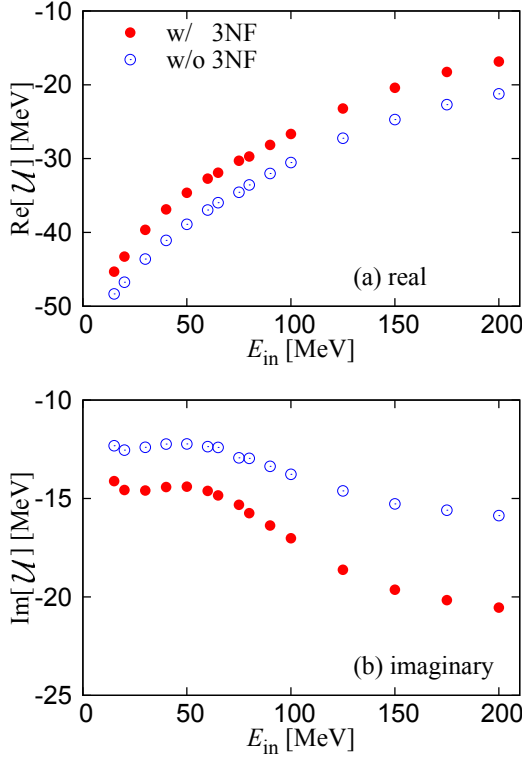


FIG. 2: (Color online) E_{in} dependence of \mathcal{U} at $k_F = 1.2 \text{ fm}^{-1}$ for the cutoff $\Lambda = 550 \text{ MeV}$. Filled (open) circles stand for the results of BHF calculations with (without) chiral 3NFs. Panels (a) and (b) correspond to the real and imaginary parts of \mathcal{U} .

spin S and isospin T of the interacting two-nucleon system. The total single-particle potential \mathcal{U} is obtained by the single-particle potential \mathcal{U}^{ST} in each (S, T) channel as

$$\mathcal{U} = \sum_{ST} (2S+1)(2T+1) \mathcal{U}^{ST}, \quad (8)$$

where \mathcal{U}^{ST} is defined by Eq. (6) with \tilde{g} replaced by \tilde{g}^{ST} .

Figure 4 shows E_{in} dependence of $U^{ST} \equiv (2S+1)(2T+1)\mathcal{U}^{ST}$ for the case of $k_F = 1.2 \text{ fm}^{-1}$. Here we do the following three kinds of BHF calculations:

- I. All kinds of chiral 3NFs, i.e., diagrams (a)-(c) in Fig. 1, are taken into account.
- II. All kinds of chiral 3NFs are switched off. Namely, Only chiral 2NF is considered.
- III. Diagrams (b) and (c) are ignored by setting $c_D = c_E = 0$ in BHF calculations. Namely, only the Fujita-Miyazawa 2π -exchange 3NF of diagram (a) is considered.

Filled circles (squares) stand for the real (imaginary) part of U^{ST} for calculation I, while open circles (squares) correspond to the real (imaginary) part of U^{ST} for calculation II; note that lines are a guide to the eye. The two

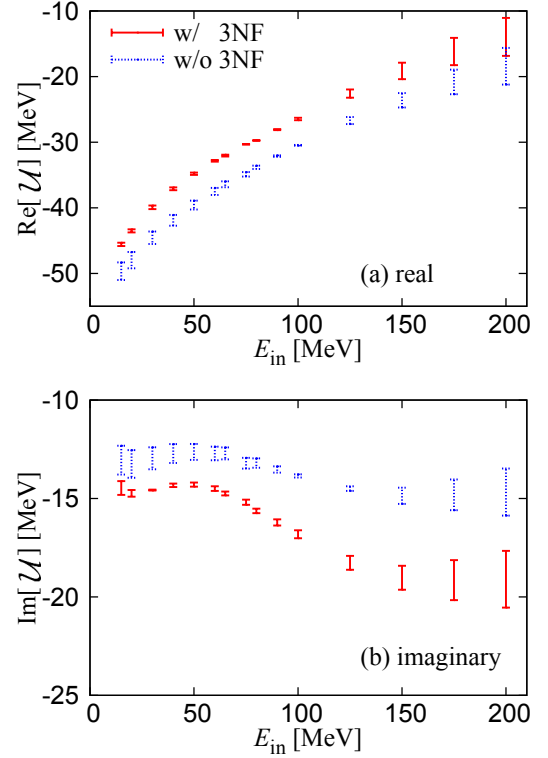


FIG. 3: (Color online) Single-particle potential \mathcal{U} as a function of E_{in} at $k_F = 1.2 \text{ fm}^{-1}$ for two cases of $\Lambda = 450, 550 \text{ MeV}$. Λ dependence is shown as an error bar. The error bar plotted by a solid (dashed) line means the results of BHF calculations with (without) chiral 3NFs. Panels (a) and (b) mean the real and imaginary parts of \mathcal{U} , respectively.

calculations show that chiral 3NF effects are significant for ${}^3\text{O}$ ($S=1, T=1$) and ${}^3\text{E}$ ($S=1, T=0$) channel and the real part of ${}^1\text{E}$ ($S=0, T=1$) channel. Small circles (squares) represent the real (imaginary) part of U^{ST} for calculation III. For ${}^3\text{E}$ and ${}^3\text{O}$, one can see from calculations II and III that chiral 3NF effects mainly come from the Fujita-Miyazawa 2π -exchange 3NF of diagram (a). For the real part of ${}^1\text{E}$ ($S=0, T=1$) channel, the effect of diagram (a) is sizable, but it is considerably reduced by the effects of diagram (b) and (c). As a net effect of these properties, chiral 3NFs make \mathcal{U} less attractive and more absorptive, and the repulsion mainly stems from diagram (a) in its ${}^3\text{O}$ component and the absorption does from diagram (a) in its ${}^3\text{O}$ and ${}^3\text{E}$ components. The chiral-3NF effects become more significant at larger incident energies. One can easily expect that these properties persist also in the optical potentials of ${}^4\text{He}$ scattering, since \mathcal{U} plays a role of “optical potential” of nucleon scattering in nuclear matter. This point will be discussed later in Sec. III.

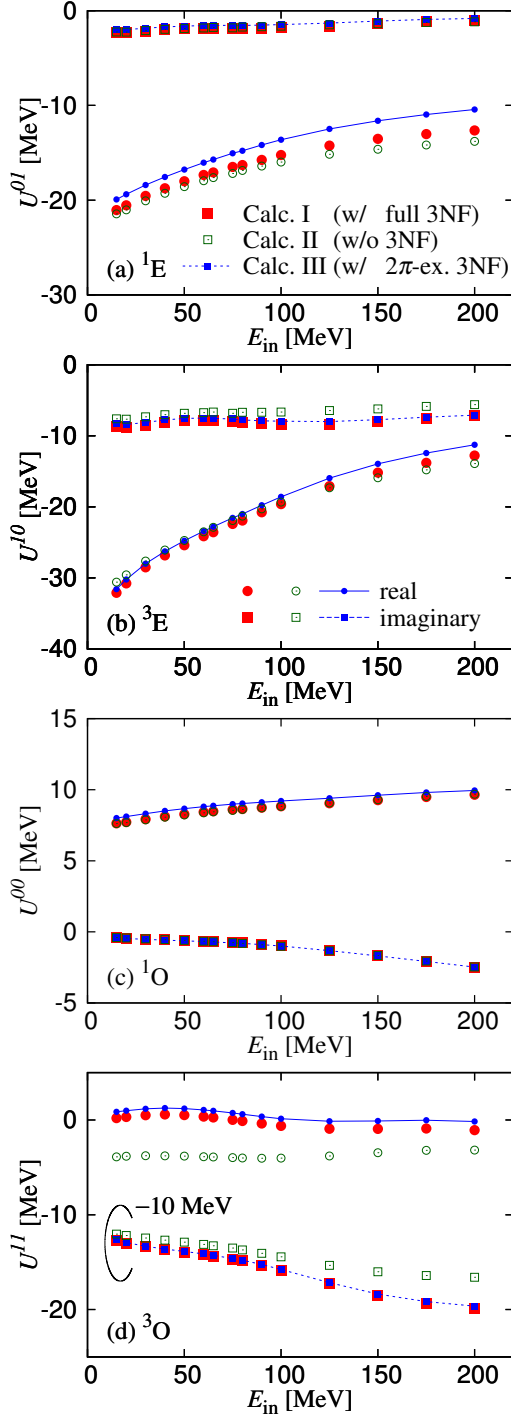


FIG. 4: (Color online) E_{in} dependence of $U^{ST} \equiv (2S+1)(2T+1)\mathcal{U}^{ST}$ at $k_F = 1.2 \text{ fm}^{-1}$ for (a) ^1E ($S = 0, T = 1$), (b) ^3E ($S = 1, T = 0$), (c) ^1O ($S = 0, T = 0$), and (d) ^3O ($S = 1, T = 1$). Filled circles (squares) represent U^{ST} in its real (imaginary) part obtained by BHF calculations with all kinds of chiral 3NFs. Open circles (squares) correspond to the real (imaginary) part of U^{ST} in which all kinds of chiral 3NFs are switched off. Lines with small circles (squares) stand for U^{ST} obtained by BHF calculations with $c_D = c_E = 0$. Note that lines are a guide to the eye; the solid (dashed) line corresponds to the real (imaginary) part. For ^3O , the imaginary part is shifted down by 10 MeV.

C. Local version of chiral g matrix

The \tilde{g} matrix $\tilde{g}(k_F, E_{\text{in}})$ of Eq.(7) is a nonlocal potential depending on k_F and E_{in} , being calculated in symmetric nuclear matter. In addition, it is obtained numerically. These properties are quite inconvenient in various applications. In order to circumvent the problem, the Melbourne group showed that elastic scattering are determined by the on-shell and near-on-shell components of g matrix [21], and provided a local version of g matrix in which the potential parameters are so determined as to reproduce the relevant components [21, 34, 35]. The Melbourne g matrix thus obtained well accounts for NN scattering in free space that corresponds to the limit of $\rho = 0$, and the Melbourne g -matrix folding model reproduces NA scattering, as already mentioned in Sec. I.

In our previous paper [25], following the Melbourne-group procedure [21, 34, 35], we succeeded in parameterizing a local version of chiral \tilde{g} matrix in a 3-range Gaussian form for each of the central, spin-orbit and tensor components. The Gaussian form makes various kinds of numerical calculations efficient. The range and strength parameters were so determined as to reproduce the on-shell and near-on-shell matrix elements of the original \tilde{g} matrix for each spin-isospin channel, k_F and E_{in} . As for the central part, the range parameters obtained were (0.4, 0.9, 2.5) in units of fm. In this paper, we repeated this procedure for E_{in} up to 200 MeV and parameterized a local version of chiral \tilde{g} matrix with good accuracy, as shown below. Since the analysis was already made at $E_{\text{in}} = 65 \text{ MeV}$ in Ref. [25], we make the same analysis for higher energies, say $E_{\text{in}} = 150 \text{ MeV}$, in this paper. Whenever we have to distinguish the two types of g matrices, we call the local version of \tilde{g} matrix “Kyushu chiral g matrix” and the original nonlocal \tilde{g} matrix “original chiral g matrix”. For the case of $E_{\text{in}} = 75 \text{ MeV}$ as an example, we present the parameter set of Kyushu chiral g matrix in Appendix A.

Figure 5 shows differential cross sections as a function of c.m. scattering angle $\theta_{\text{c.m.}}$ for $p+n$ scattering at $E_{\text{in}} = 150 \text{ MeV}$ in free space, i.e., in the limit of $\rho = 0$. The solid and dashed lines denote the results of original and Kyushu chiral t matrices, respectively; note that the g matrix is reduced to the t matrix in the limit of $\rho = 0$. The Kyushu chiral t matrix reproduces the result of original chiral t matrix well.

Figure 6 shows k_F dependence of U^{ST} at $E_{\text{in}} = 150 \text{ MeV}$. Both 2NF and 3NF are taken into account in BHF calculations. The filled circles (squares) denote the results of the real (imaginary) part of original chiral g matrix, whereas the solid (dashed) lines correspond to the real (imaginary) part of Kyushu chiral g matrix. The range $k_F \lesssim 1.35 \text{ fm}^{-1}$ ($\rho \lesssim \rho_0$) contributes to the optical potentials of ^4He scattering, when the potentials are constructed by the folding model explained in Sec. II D. In particular, the Fermi momentum $k_F \approx 1.2 \text{ fm}^{-1}$, corresponding to the peripheral region of the optical potentials, is important for the elastic scattering. The Kyushu

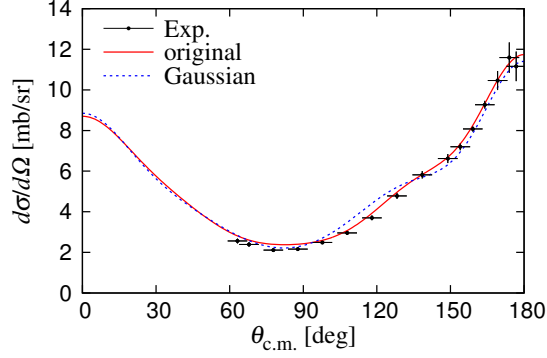


FIG. 5: (Color online) Differential cross sections for $p+n$ scattering at $E_{\text{in}} = 150$ MeV in free space. Here $\theta_{\text{c.m.}}$ denotes the scattering angle in the center of mass system. The solid line stands for the result of original chiral t matrix, while the dashed line corresponds to the result of Kyushu chiral t matrix (the local version of chiral t matrix). Experimental data are taken from Ref. [36].

chiral g matrix well reproduces the results of the original chiral g matrix.

D. Folding model

In this paper, the optical potentials are derived by folding Kyushu chiral g matrix with ρ_P and ρ_T for ^4He scattering on ^{208}Pb , ^{58}Ni and ^{40}Ca targets. In general, the folding potential is referred to as a double-folding (DF) model for AA scattering, while it is called a single-folding (SF) model for NA scattering.

In the g -matrix SF model for NA elastic scattering, the so-called local-density approximation is taken, that is, the value of ρ in $g(\rho)$ is identified with the value of ρ_T at the midpoint \mathbf{r}_m of interacting two nucleons: $\rho = \rho_T(\mathbf{r}_m)$. Target-excitation effects on the elastic scattering are well taken into account by this framework. In fact, the Melbourne g -matrix SF model succeeded in reproducing NA scattering [21]. In our previous work [25], furthermore, we showed that the Kyushu chiral g -matrix SF model also well accounted for proton scattering at $E_{\text{in}} = 65$ MeV and chiral-3NF effects are small there.

The g -matrix DF model for AA scattering had a problem to be settled. In order to obtain the g matrix applicable for AA scattering, in principle, we have to consider two Fermi spheres in nuclear-matter calculations and solve a collision between a nucleon in the first Fermi sphere and a nucleon in the second one [37, 38]. However, actual calculations are not feasible. In fact, all the g matrices provided so far were obtained by assuming a single Fermi sphere and solving nucleon scattering on the Fermi sphere. For consistency with the nuclear-matter calculation, we assumed $\rho = \rho_T(\mathbf{r}_m)$ in $g(\rho)$ and applied the framework to $^3,4\text{He}$ scattering in a wide energy range of $30 \lesssim E_{\text{in}}/A_P \lesssim 180$ MeV [29, 31]. The Melbourne

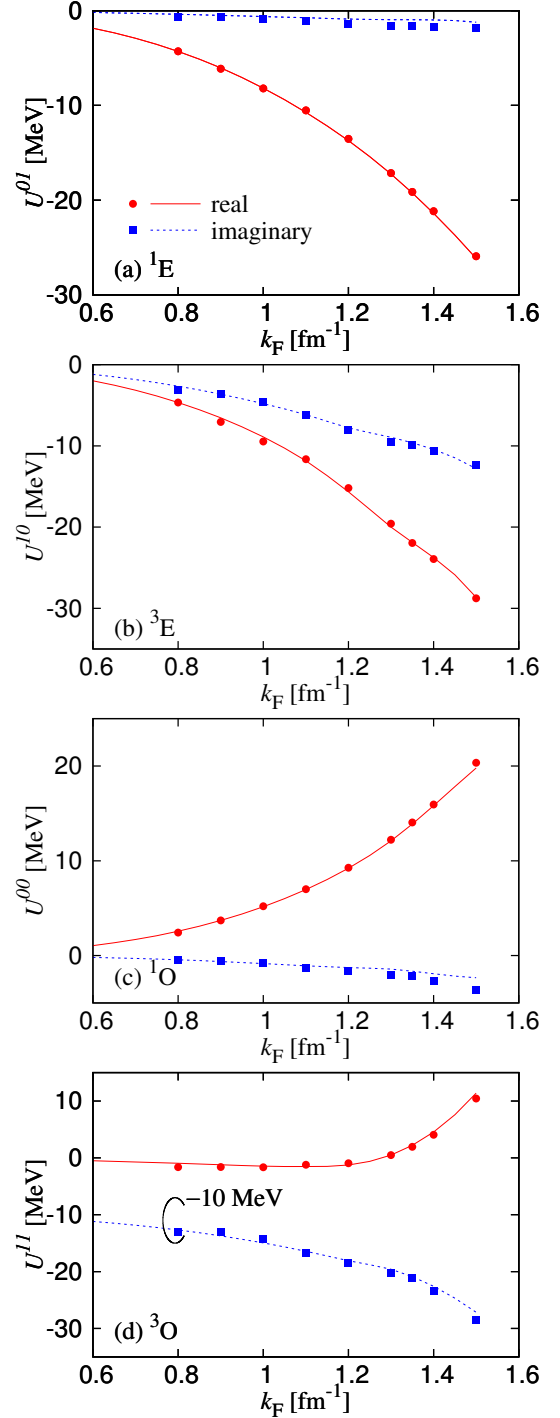


FIG. 6: (Color online) k_F dependence of U^{ST} at $E_{\text{in}} = 150$ MeV for (a) ^1E , (b) ^3E , (c) ^1O , and (d) ^3O . Here 3NFs are taken into account in BHF calculations. The filled circles (squares) stand for the results of the real (imaginary) part of original chiral g matrix, while the solid (dashed) lines correspond to the results of the real (imaginary) part of Kyushu chiral g matrix. For ^3O , the imaginary part is shifted down by 10 MeV.

g -matrix DF model based on the target-density approximation (TDA) well accounted for $^3,^4\text{He}$ scattering, particularly for forward differential cross sections where 3NF effects are considered to be negligible [22, 23, 26]. In our previous analysis [25], the DF-TDA model based on Kyushu chiral g matrix well explained ^4He scattering at $E_{\text{in}}/A_{\text{P}} \approx 72$ MeV. We then take the DF-TDA model for ^4He scattering in this paper throughout all the incident energies $30 \lesssim E_{\text{in}}/A_{\text{P}} \lesssim 180$ MeV where the experimental data are available.

The DF model naturally treats both the direct and knock-on exchange processes [38–40]. In the latter process, interacting two nucleons are exchanged and thereby the potential becomes nonlocal. However, the nonlocality can be localized with high accuracy by the local momentum approximation [20], as proven in Refs. [41, 42]. The folding potential $U(R)$ thus obtained is a function of the distance R between P and T;

$$U(R) = \sum_{\mu\nu} \int d\mathbf{r}_{\text{P}} \int d\mathbf{r}_{\text{T}} \rho_{\text{P}}^{(\mu)}(r_{\text{P}}) \rho_{\text{T}}^{(\nu)}(r_{\text{T}}) \times \tilde{g}_{\mu\nu}^{\text{DR}}(s, E_{\text{in}}/A_{\text{P}}; \rho) - \sum_{\mu\nu} \int d\mathbf{r}_{\text{P}} \int d\mathbf{r}_{\text{T}} \tilde{\rho}_{\text{P}}^{(\mu)}(\mathbf{r}_{\text{P}}, \mathbf{s}) \tilde{\rho}_{\text{T}}^{(\nu)}(\mathbf{r}_{\text{T}}, \mathbf{s}) \times \tilde{g}_{\mu\nu}^{\text{EX}}(s, E_{\text{in}}/A_{\text{P}}; \rho) j_0\left(\frac{A_{\text{P}}+A_{\text{T}}}{A_{\text{P}}A_{\text{T}}} K(R)s\right), \quad (9)$$

where the indices μ and ν are the isospin of corresponding nucleon and $\mathbf{s} = \mathbf{r}_{\text{T}} - \mathbf{r}_{\text{P}} - \mathbf{R}$ is the coordinate between interacting two nucleons. The densities $\rho_{\text{P(T)}}$ and $\tilde{\rho}_{\text{P(T)}}$ represent the one-body and mixed densities of P (T);

$$\tilde{\rho}_{\text{P(T)}} = \rho_{\text{P(T)}}(|\mathbf{r}_{\text{P(T)}} \pm \mathbf{s}/2|) \frac{3j_1(k_{\text{F}}^{\text{P(T)}} s)}{k_{\text{F}}^{\text{P(T)}} s}. \quad (10)$$

The Fermi momentum $k_{\text{F}}^{\text{P(T)}}$ is related to the density $\rho_{\text{P(T)}}$. The direct (exchange) term of g -matrix $\tilde{g}_{\mu\nu}^{\text{DR(EX)}}$ is defined by \tilde{g}^{ST} as

$$\tilde{g}_{pp,nn}^{\text{DR(EX)}} = \frac{1}{4}(\pm \tilde{g}^{01} + 3\tilde{g}^{11}), \quad (11)$$

$$\tilde{g}_{pn,np}^{\text{DR(EX)}} = \frac{1}{8}(\tilde{g}^{00} \pm \tilde{g}^{01} \pm 3\tilde{g}^{10} + 3\tilde{g}^{11}). \quad (12)$$

See Refs. [26, 31, 43, 44] for the detail of the formulation of the DF model. The S matrices for ^4He elastic scattering are obtained by solving the one-body Schrödinger equation with $U(R)$.

For the targets ^{208}Pb and ^{58}Ni , the matter densities ρ_{T} are evaluated by the spherical Hartree-Fock (HF) method based on the Gogny-D1S interaction [45], where the spurious c.m. motions are removed with the standard manner [46]. For the projectile ^4He and the target ^{40}Ca , we take the phenomenological proton-density determined from electron scattering [47]; here the finite-size effect of proton charge is unfolded with the standard procedure [48], and the neutron density is assumed to have

the same geometry as the proton one, since the difference between the neutron root-mean-square radius and the proton one is only 1% in spherical HF calculations.

III. RESULTS

Now we analyze ^4He elastic scattering on nuclei systematically in a wide range $E_{\text{in}}/A_{\text{P}} = 26\text{--}175$ MeV. Here heavier targets ^{208}Pb , ^{58}Ni and ^{40}Ca are considered, because the g matrix is calculated in nuclear matter and thereby the g -matrix DF model is expected to be more reliable for heavier targets.

Figure 7 shows differential cross sections $d\sigma/d\Omega$ as a function of transfer momentum q for ^4He scattering from a ^{208}Pb target in $E_{\text{in}}/A_{\text{P}} = 26\text{--}175$ MeV where the experimental data are available. The solid and dashed lines stand for the results of the Kyushu chiral g -matrix DF model with and without 3NF effects, respectively. Chiral 3NFs improve the agreement of the theoretical results with the experimental data. Particularly for $E_{\text{in}}/A_{\text{P}} \gtrsim 100$ MeV, the agreement is pretty good. We can observe the same features also for ^{58}Ni and ^{40}Ca targets, as shown in Figs. 8 and 9, although there is a tendency that the agreement becomes better as the target mass increases.

Now we analyze effects of Fujita-Miyazawa 2π -exchange 3NF on differential cross sections $d\sigma/d\Omega$ for $^4\text{He}+^{58}\text{Ni}$ scattering. In Fig 10, the solid, dashed and dot-dashed lines denote the results of calculations I, II and III, respectively; see Sec. II B for the definition of g -matrix calculations. The difference between calculations I and II means effects of all 3NFs, and that between calculations II and III corresponds to effects of Fujita-Miyazawa 2π -exchange 3NF. The resultant cross sections show that the Fujita-Miyazawa 2π -exchange 3NF is the main contribution of chiral-3NF effects on ^4He scattering.

Figure 11 shows the R dependence of the optical potentials $U(R)$ for ^4He elastic scattering from a ^{58}Ni target at $E_{\text{in}}/A_{\text{P}} = 26, 60$ and 175 MeV. The solid and dashed lines represent the $U(R)$ with and without chiral-3NF effects; note that only the central potential is generated by the DF-TDA model. As expected, chiral-3NF effects make repulsive and absorptive corrections to the optical potentials, and the corrections slightly increase as E_{in} goes up; note that the effects hardly depend on E_{in} in the peripheral region, $R \approx 6$ fm, that is important for the elastic scattering. As already mentioned in Sec. II B, the repulsive correction mainly comes from the Fujita-Miyazawa 2π -exchange 3NF in its ^3O component, and the absorptive correction stems from the ^3E and ^3O components of Fujita-Miyazawa 2π -exchange 3NF.

Figure 12 shows the uncertainty coming from Λ dependence of differential cross sections $d\sigma/d\Omega$ for $^4\text{He}+^{58}\text{Ni}$ elastic scattering. Here two cases of $\Lambda = 550$ and 450 MeV are considered. Λ dependence is shown by a hatching for each of 2NF and 2NF+3NF calculations; note that the hatching region surrounded by solid (dashed)

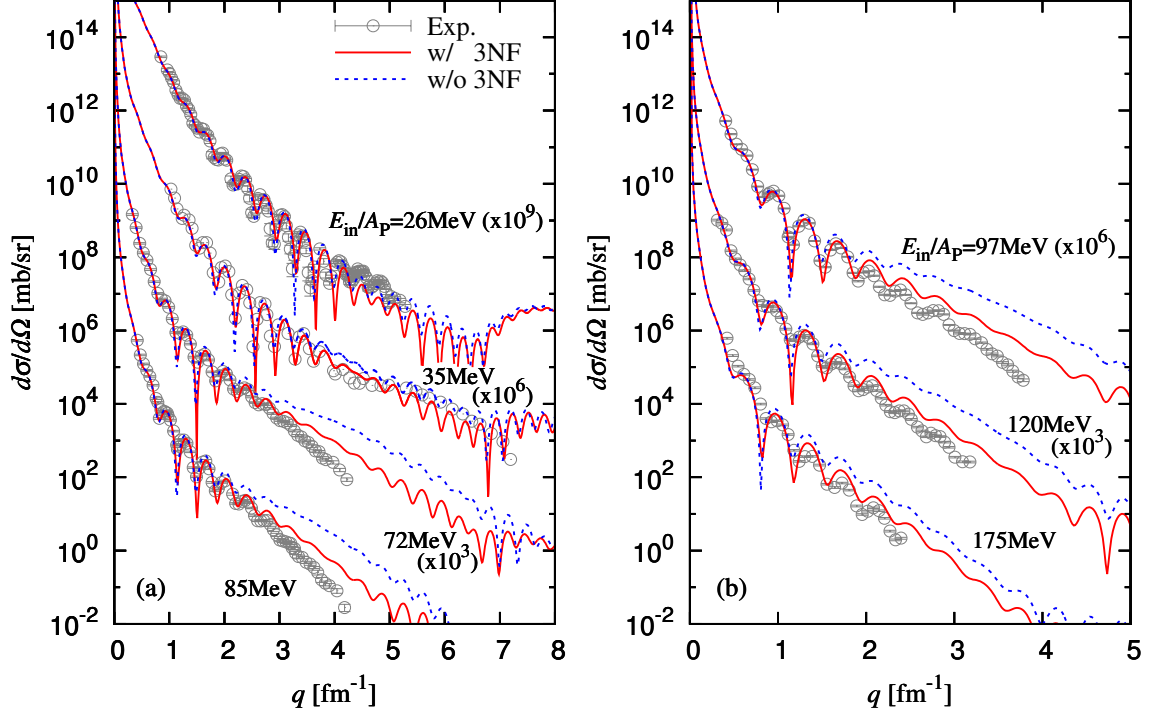


FIG. 7: (Color online) Differential cross sections $d\sigma/d\Omega$ as a function of transfer momentum q for ${}^4\text{He}$ scattering from a ${}^{208}\text{Pb}$ target at $E_{\text{in}}/A_{\text{P}} = 26\text{--}175$ MeV. The solid (dashed) lines denote the results of Kyushu chiral g matrix with (without) 3NF effects. Each cross section is multiplied by the factor shown in the figure. Experimental data are taken from Refs. [49–52].

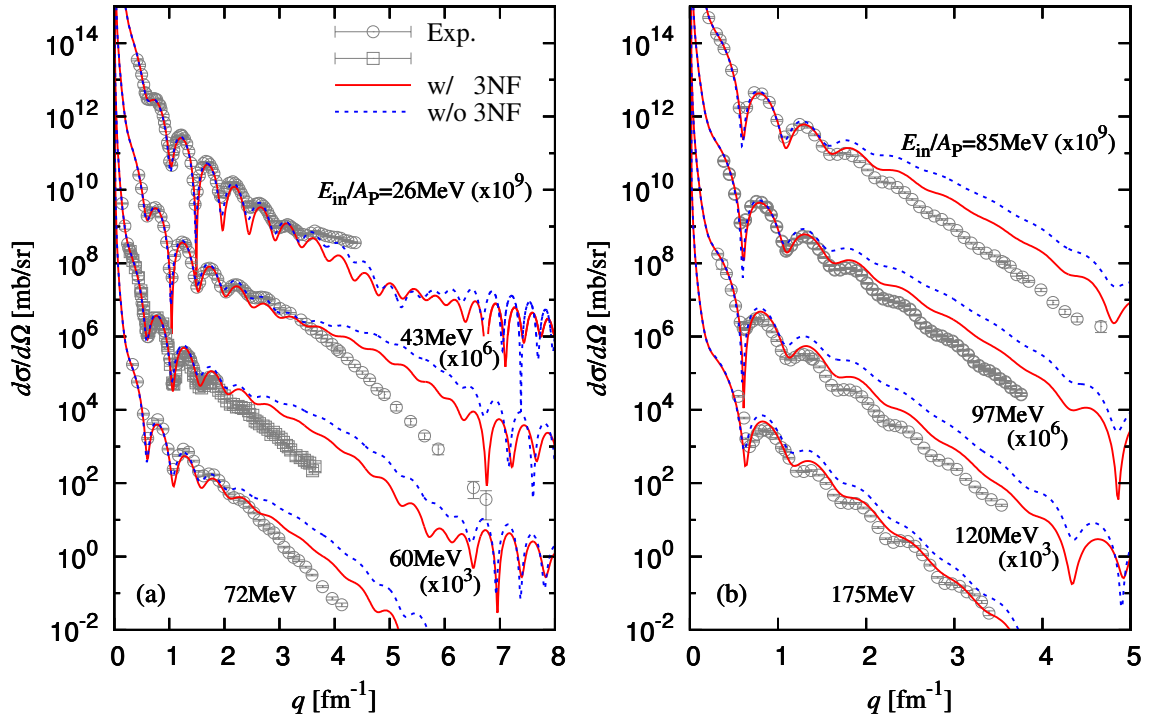


FIG. 8: (Color online) Same as Fig. 7, but the target nucleus is ${}^{58}\text{Ni}$. Experimental data are taken from Refs. [51, 53–57].

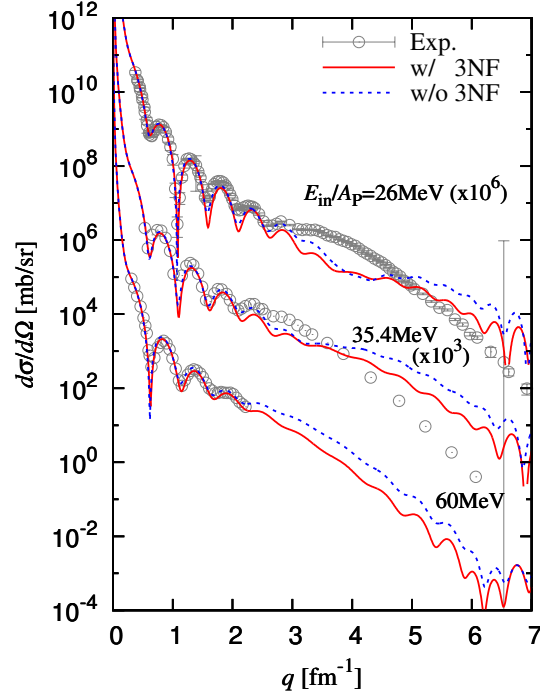


FIG. 9: (Color online) Same as Fig. 7, but the target nucleus is ^{40}Ca . Experimental data are taken from Refs. [49, 58, 59].

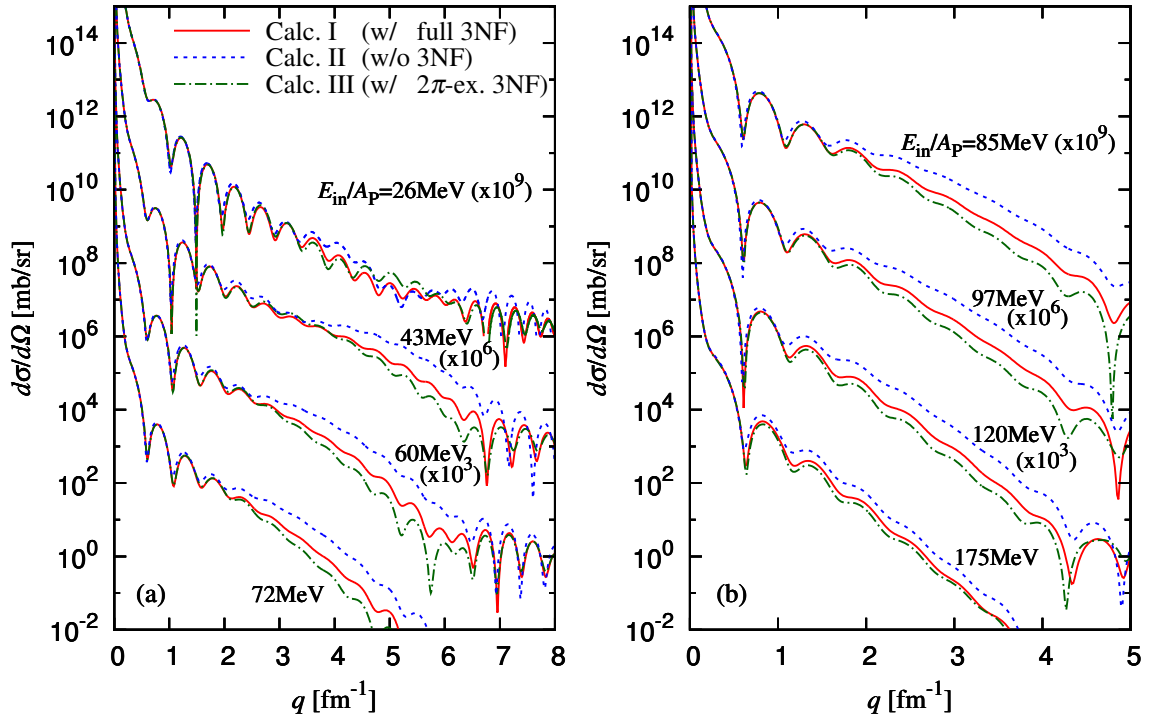


FIG. 10: (Color online) Effects of Fujita-Miyazawa 2π -exchange 3NF on differential cross sections $d\sigma/d\Omega$ for $^4\text{He} + ^{58}\text{Ni}$ scattering, where q is the transfer momentum. The solid and dashed lines denote the results of calculations I and II, respectively, and the dot-dashed line corresponds to the results of calculations III; see Sec. II B for the definition of g -matrix calculations. Each cross section is multiplied by the factor shown in the figure.

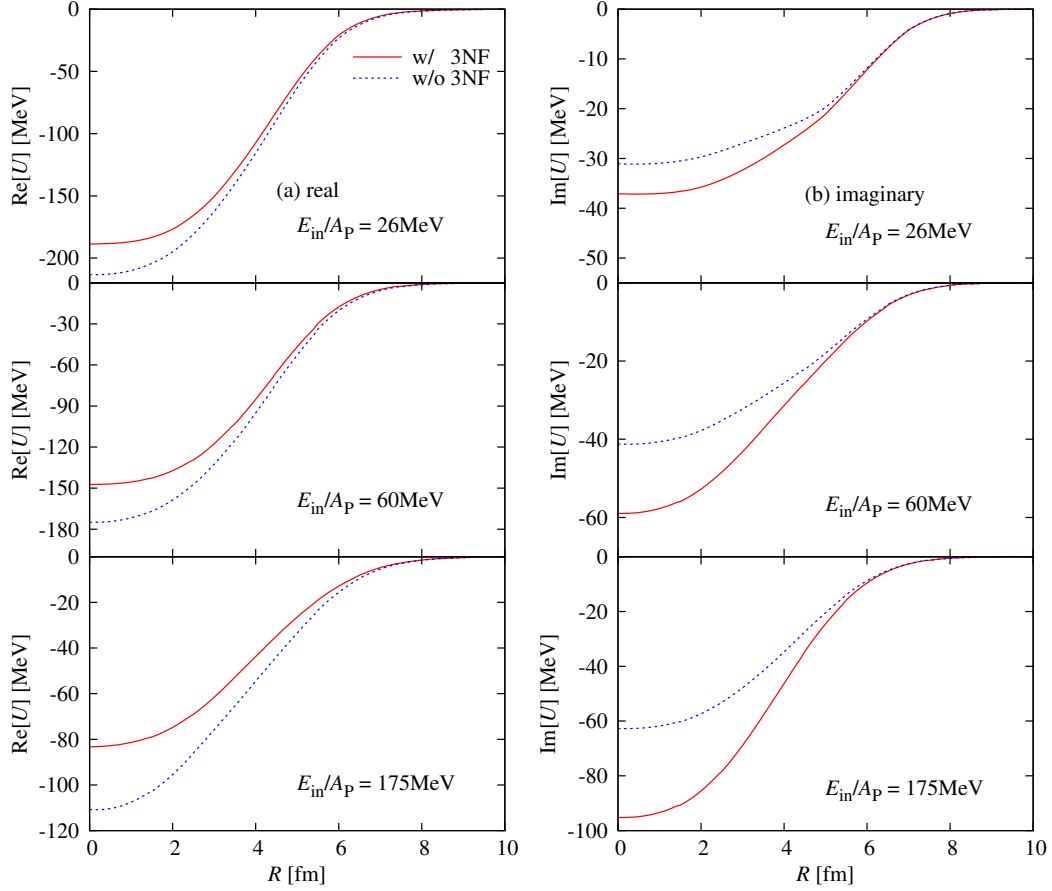


FIG. 11: (Color online) Optical potentials $U(R)$ as a function of R for ${}^4\text{He}+{}^{58}\text{Ni}$ elastic scattering at $E_{\text{in}}/A_{\text{P}}=26, 60$ and 175 MeV. The solid (dashed) lines denote the optical potentials with (without) chiral-3NF effects. Panels (a) and (b) represent the real and imaginary parts of U , respectively.

lines means the uncertainty coming from Λ dependence for 2NF+3NF (2NF) calculations. As expected, Λ dependence becomes larger as E_{in} increases, but the uncertainty coming from Λ dependence is still smaller than chiral-3NF effects, even at $E_{\text{in}}/A_{\text{P}} = 175$ MeV.

The scattering amplitude can be decomposed into the near- and far-side components [60]. As illustrated in Fig. 13, these components are well defined, when outgoing waves are generated only in the peripheral region of T. ${}^4\text{He}$ scattering on a heavier target is a good case. The absorptive correction of chiral-3NF effects makes the decomposition more applicable. The decomposition is a convenient tool for investigating the interplay between differential cross sections $d\sigma/d\Omega$ and the real part of $U(R)$. The near-side (far-side) outgoing waves are mainly induced by repulsive Coulomb (attractive nuclear) force, so that very-forward-angle (middle-angle) scattering are dominated by the near-side (far-side) components. As a consequence of this property, a large interference pattern appears in differential cross sections at the forward angles where the two components become comparable, and the far-side dominance is realized at middle angles af-

ter the interference pattern. In the middle angle region, any repulsive correction to $U(R)$ reduces differential cross sections.

Figure 14 shows the near/far decomposition of differential cross sections $d\sigma/d\Omega$ for ${}^4\text{He}+{}^{58}\text{Ni}$ scattering at $E_{\text{in}}/A_{\text{P}} = 72$ MeV. The dotted and dashed lines represent the near- and far-side cross sections, respectively, and the solid line denotes differential cross sections before the near/far decomposition; here chiral-3NF effects are taken into account. The solid line shows a large interference pattern at $\theta_{\text{c.m.}} = 5\text{--}15^\circ$, and the solid line agrees with the dashed one in $20^\circ \lesssim \theta_{\text{c.m.}} \lesssim 40^\circ$. The far-side dominance is thus realized in middle angles $20^\circ \lesssim \theta_{\text{c.m.}} \lesssim 40^\circ$. The far-side dominance in $20^\circ \lesssim \theta_{\text{c.m.}} \lesssim 40^\circ$ persists, even after chiral 3NFs are switched off. The dot-dashed line is the far-side cross section in which chiral 3NFs are switched off. The repulsive correction coming from chiral 3NFs suppresses differential cross sections in far-side dominant angles $20^\circ \lesssim \theta_{\text{c.m.}} \lesssim 40^\circ$ from the dot-dashed line to the solid (dashed) line. Thus, chiral-3NF effects become more visible in the far-side dominant angle region.

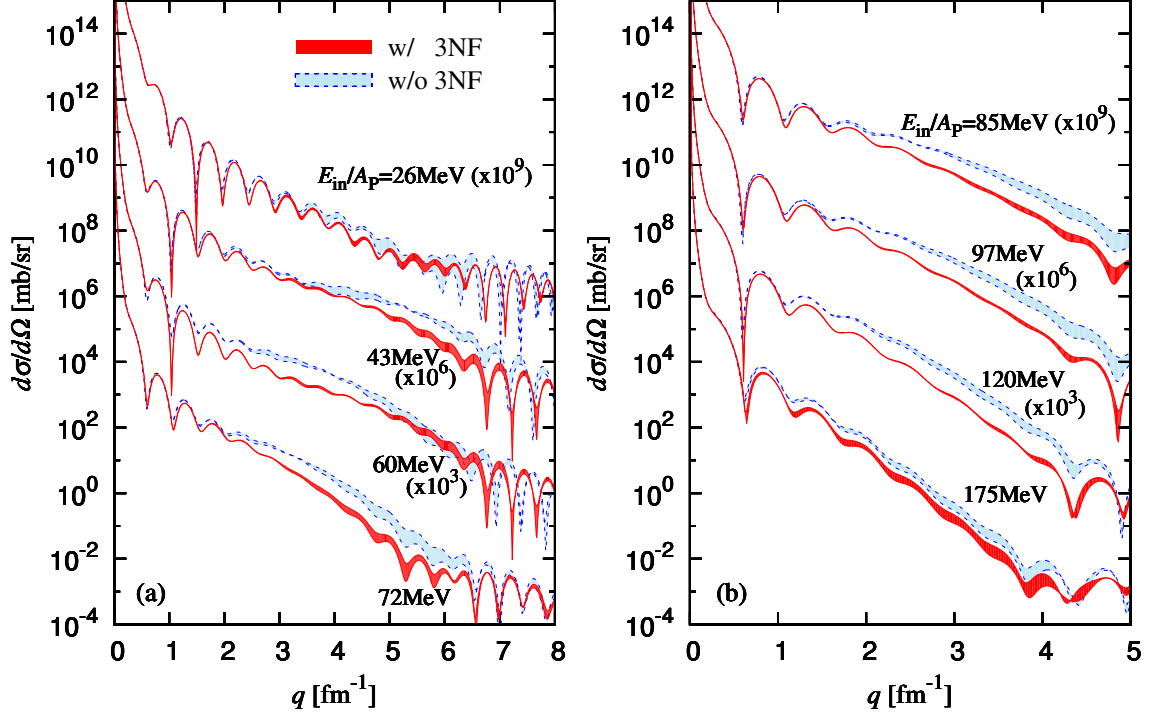


FIG. 12: (Color online) Uncertainty coming from Λ dependence of differential cross sections $d\sigma/d\Omega$ for ${}^4\text{He}+{}^{58}\text{Ni}$ elastic scattering. Λ dependence is drawn by a hatching for each of 2NF and 2NF+3NF calculations, where two cases of $\Lambda = 550$ and 450 MeV are taken. Note that the hatching region surrounded by the solid (dashed) lines corresponds to the uncertainty coming from Λ dependence for 2NF+3NF (2NF) calculations.

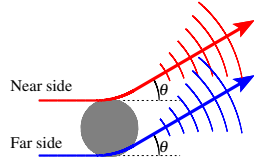


FIG. 13: (Color online) Illustration of the near/far decomposition.

Finally, we comment on chiral-3NF effects on total reaction cross sections σ_R briefly. Radii of stable and unstable nuclei are often determined from measured σ_R with the folding model and/or the Glauber model. Figure 15 shows σ_R as a function of E_{in}/A_P for ${}^4\text{He}$ scattering on ${}^{58}\text{Ni}$ and ${}^{208}\text{Pb}$ targets. Closed circles (squares) mean the results of Kyushu chiral g matrix with (without) 3NF effects. The two kinds of results are close to each other, indicating that chiral-3NF effects are negligible for σ_R . The fact ensures that the determination of nuclear radii from measured σ_R is reliable.

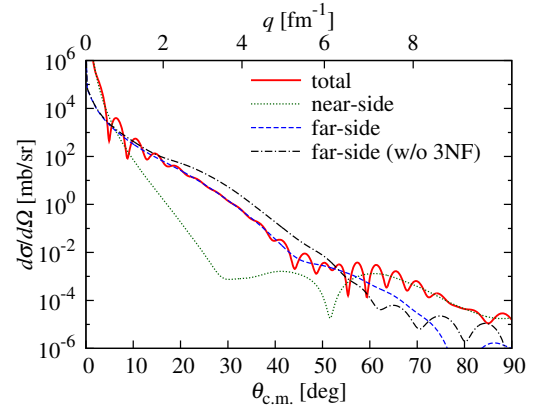


FIG. 14: (Color online) Near/far decomposition of differential cross sections $d\sigma/d\Omega$ for ${}^4\text{He}+{}^{58}\text{Ni}$ scattering at $E_{\text{in}}/A_P = 72$ MeV. The dotted (dashed) line stands for the near-side (far-side) cross sections, while the solid line denotes differential cross sections before the near/far decomposition; here chiral-3NF effects are taken into account. The dot-dashed line corresponds to the far-side cross section in which chiral 3NFs are switched off.

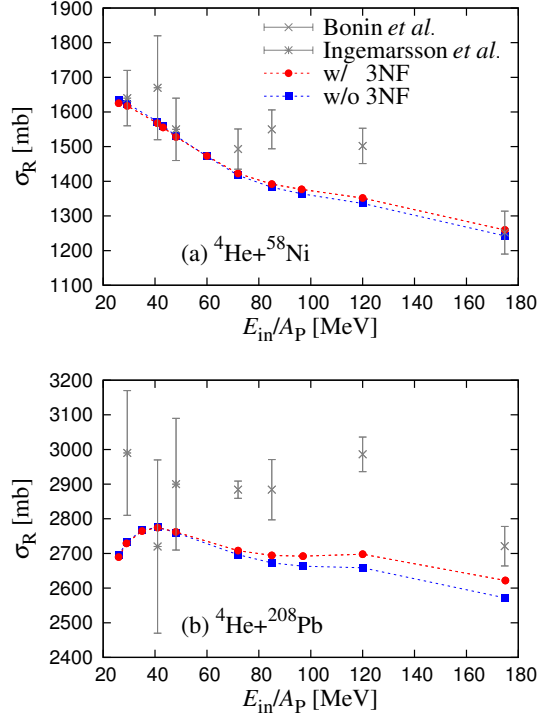


FIG. 15: (Color online) Total reaction cross sections σ_R as a function of E_{in} for ${}^4\text{He}$ scattering on (a) ${}^{58}\text{Ni}$ and (b) ${}^{208}\text{Pb}$ targets. Closed circles (squares) denote the results of Kyushu chiral g matrix with (without) 3NF effects. Experimental data are taken from Refs. [61, 62].

IV. SUMMARY

We investigated basic properties of chiral 3NFs in symmetric nuclear matter with positive energies up to 200 MeV by using the BHF method with chiral 2NFs of N^3LO and chiral 3NFs of NNLO in the Bochum-Bonn-Jülich [33], parameterization, and analyzed chiral-3NF effects on ${}^4\text{He}$ elastic scattering from heavier targets ${}^{208}\text{Pb}$, ${}^{58}\text{Ni}$ and ${}^{40}\text{Ca}$ over a wide incident-energy range of $30 \lesssim E_{in}/A_P \lesssim 200$ MeV by the Kyushu chiral g -matrix folding model.

First, we summarize the basic properties of chiral 3NFs in symmetric nuclear matter with positive energies E_{in} up to 200 MeV:

- (1) Chiral 3NFs make the single-particle potential \mathcal{U} less attractive and more absorptive.
- (2) The repulsive and absorptive corrections slightly increase as E_{in} goes up.
- (3) Chiral 3NF effects on \mathcal{U} mainly come from the Fujita-Miyazawa 2π -exchange 3NF (diagram (a) in Fig. 1). More precisely, the repulsion mainly stems from the ${}^3\text{O}$ component of the diagram (a) and the absorption does from the ${}^3\text{O}$ and ${}^3\text{E}$ components of the diagram (a).

Properties (1)-(3) persist in the optical potential of ${}^4\text{He}$ scattering. This is natural, since the single-particle potential plays a role of the optical potential in nuclear matter. However, it should be noted that chiral-3NF effects depend little on E_{in} in the peripheral region that is important for the elastic scattering.

Chiral-3NF effects are evident for ${}^4\text{He}$ scattering in $E_{in}/A_P \gtrsim 60$ MeV at the middle angles where the cross sections are dominated by the far-side component of the scattering amplitude. The repulsive correction of chiral 3NFs reduces the far-side component and thereby yields better agreement with the experimental data. Eventually, the Kyushu chiral g -matrix DF model reproduces measured differential cross sections pretty well, particularly for ${}^4\text{He}$ scattering at $E_{in}/A_P \gtrsim 100$ MeV.

All the analyses mentioned above were made with $\Lambda = 550$ MeV. In order to investigate Λ dependence in nuclear-matter and ${}^4\text{He}$ -scattering calculations, we take $\Lambda = 450$ MeV in addition to $\Lambda = 550$ MeV. The uncertainty coming from Λ dependence is smaller than chiral-3NF effects. There is a tendency that the uncertainty becomes larger as E_{in} increases, but it is still smaller than chiral-3NF effects even at $E_{in} = 175$ MeV.

Finally, we provide the local version of chiral g -matrix with a 3-range Gaussian form for the case of $E_{in} = 72$ MeV. Numerical numbers are presented in Appendix A. This local version of chiral g matrix strongly encourages us to use it for studying various kinds of nuclear reactions.

Acknowledgements

The authors would like to thank K. Ogata and K. Minomo for valuable discussions on localization of the chiral g -matrix and the reaction analyses. This work is supported in part by Grant-in-Aid for Scientific Research (Nos. 25400266, 26400278, 16K05353, and 16J00630) from Japan Society for the Promotion of Science (JSPS).

Appendix A: Parameter set of Kyushu chiral g matrix

In this Appendix, we provide the central part of the Kyushu chiral g matrix, for the case of $E_{in}/A_P = 75$ MeV, in a 3-range Gaussian form

$$g^{ST}(s, k_F, E_{in}/A_P) = \sum_{i=1}^3 g_i^{ST}(k_F, E_{in}/A_P) e^{-s^2/\lambda_i^2} \quad (\text{A1})$$

in each (S, T) channel. The range parameters are fixed to be $(\lambda_1, \lambda_2, \lambda_3) = (0.4, 0.9, 2.5)$ in units of fm, and the strength parameters $\tilde{g}_i^{ST}(k_F, E_{in}/A_P)$ in units of MeV, which include chiral 3NF effects, are tabulated in Tables I-IV for six cases of the Fermi momentum k_F . We will publish parameter sets of other cases on the website [63].

TABLE I: Singlet-even ($S = 0, T = 1$) component of Kyushu chiral g matrix for the incident energy $E_{\text{in}}/A_P = 75$ MeV. The range parameters are fixed to be $(\lambda_1, \lambda_2, \lambda_3) = (0.4, 0.9, 2.5)$ in units of fm. Entries are in MeV, but k_F is presented in units of fm^{-1} .

k_F	real part			imaginary part		
	$i = 1$	$i = 2$	$i = 3$	$i = 1$	$i = 2$	$i = 3$
0.00	1.78627×10^3	-2.70833×10^2	-4.08777×10^0	2.16654×10^3	-3.13038×10^2	1.39295×10^0
0.60	1.47941×10^3	-2.47638×10^2	-3.68242×10^0	1.13963×10^3	-1.71777×10^2	8.14716×10^{-1}
0.80	1.36782×10^3	-2.39203×10^2	-3.53502×10^0	7.66206×10^2	-1.20410×10^2	6.04451×10^{-1}
1.10	1.20044×10^3	-2.26551×10^2	-3.31392×10^0	2.06075×10^2	-4.33587×10^1	2.89052×10^{-1}
1.20	1.09716×10^3	-2.13700×10^2	-3.19454×10^0	1.25689×10^2	-2.88651×10^1	1.74997×10^{-1}
1.30	9.54436×10^2	-1.94839×10^2	-3.14638×10^0	6.90248×10^1	-1.93121×10^1	9.44602×10^{-2}
1.40	7.65583×10^2	-1.68406×10^2	-3.19684×10^0	1.85011×10^1	-1.05755×10^1	2.29847×10^{-2}
1.50	5.88265×10^2	-1.44596×10^2	-3.21499×10^0	-1.57455×10^0	-7.13793×10^0	-1.93808×10^{-3}

TABLE II: Triplet-even ($S = 1, T = 0$) component of Kyushu chiral g matrix for the incident energy $E_{\text{in}}/A_P = 75$ MeV. See Table I for the detail.

k_F	real part			imaginary part		
	$i = 1$	$i = 2$	$i = 3$	$i = 1$	$i = 2$	$i = 3$
0.00	1.25135×10^3	-2.14233×10^2	-4.23044×10^0	2.83713×10^3	-4.39936×10^2	-7.11017×10^{-1}
0.60	1.26094×10^3	-2.62345×10^2	-3.04629×10^0	1.96817×10^3	-3.18594×10^2	-4.36898×10^{-1}
0.80	1.26443×10^3	-2.79841×10^2	-2.61569×10^0	1.65218×10^3	-2.74470×10^2	-3.37218×10^{-1}
1.10	1.26966×10^3	-3.06084×10^2	-1.96978×10^0	1.17821×10^3	-2.08284×10^2	-1.87698×10^{-1}
1.20	1.13634×10^3	-2.90035×10^2	-1.65944×10^0	9.55010×10^2	-1.67104×10^2	-3.11895×10^{-1}
1.30	9.50006×10^2	-2.63272×10^2	-1.57370×10^0	8.52716×10^2	-1.48093×10^2	-4.61621×10^{-1}
1.40	5.98320×10^2	-2.11212×10^2	-1.85361×10^0	8.38254×10^2	-1.45648×10^2	-5.53945×10^{-1}
1.50	4.87230×10^2	-1.95265×10^2	-1.99886×10^0	8.31225×10^2	-1.43294×10^2	-6.62903×10^{-1}

TABLE III: Singlet-odd ($S = 0, T = 0$) component of Kyushu chiral g matrix for the incident energy $E_{\text{in}}/A_P = 75$ MeV. See Table I for the detail.

k_F	real part			imaginary part		
	$i = 1$	$i = 2$	$i = 3$	$i = 1$	$i = 2$	$i = 3$
0.00	1.17797×10^3	1.54048×10^1	9.23703×10^0	6.01921×10^2	-6.69649×10^1	-3.21021×10^{-1}
0.60	2.92329×10^2	9.73676×10^1	8.54387×10^0	4.56013×10^2	-5.19773×10^1	-1.83729×10^{-1}
0.80	-2.97222×10^1	1.27172×10^2	8.29181×10^0	4.02955×10^2	-4.65273×10^1	-1.33805×10^{-1}
1.10	-5.12800×10^2	1.71879×10^2	7.91372×10^0	3.23369×10^2	-3.83522×10^1	-5.89192×10^{-2}
1.20	-6.98327×10^2	1.94038×10^2	7.80370×10^0	3.02061×10^2	-3.67462×10^1	-4.49149×10^{-2}
1.30	-8.68590×10^2	2.13672×10^2	7.65323×10^0	3.08332×10^2	-3.85626×10^1	-3.61166×10^{-2}
1.40	-1.21630×10^3	2.43679×10^2	7.28544×10^0	3.39578×10^2	-4.29750×10^1	-1.70789×10^{-2}
1.50	-1.35278×10^3	2.58695×10^2	7.07301×10^0	3.38596×10^2	-4.29790×10^1	-8.86515×10^{-3}

TABLE IV: Triplet-odd ($S = 1, T = 1$) component of Kyushu chiral g matrix for the incident energy $E_{\text{in}}/A_P = 75$ MeV. See Table I for the detail.

k_F	real part			imaginary part		
	$i = 1$	$i = 2$	$i = 3$	$i = 1$	$i = 2$	$i = 3$
0.00	1.48087×10^3	-1.17015×10^2	4.09818×10^{-1}	6.26964×10^2	-5.48253×10^1	-2.34394×10^{-1}
0.60	9.89803×10^2	-7.76051×10^1	3.97949×10^{-1}	4.90110×10^2	-4.36088×10^1	-1.27683×10^{-1}
0.80	8.11232×10^2	-6.32740×10^1	3.93633×10^{-1}	4.40345×10^2	-3.95300×10^1	-8.88792×10^{-2}
1.10	5.43375×10^2	-4.17774×10^1	3.87159×10^{-1}	3.65697×10^2	-3.34119×10^1	-3.06733×10^{-2}
1.20	3.30284×10^2	-2.25888×10^1	3.93880×10^{-1}	3.57729×10^2	-3.29841×10^1	-1.48011×10^{-2}
1.30	1.31873×10^2	-4.61127×10^0	3.96357×10^{-1}	3.94174×10^2	-3.67176×10^1	-2.33502×10^{-3}
1.40	-9.73856×10^1	1.42601×10^1	3.20402×10^{-1}	4.67099×10^2	-4.37829×10^1	2.27706×10^{-2}
1.50	-2.46017×10^2	2.76700×10^1	3.11786×10^{-1}	5.04428×10^2	-4.77850×10^1	3.25825×10^{-2}

-
- [1] J. Fujita and H. Miyazawa, Prog. Theor. Phys. **17**, 360 (1957); *ibid.* **17**, 366 (1957).
- [2] R. B. Wiringa and S. C. Pieper, Phys. Rev. Lett. **89**, 182501 (2002).
- [3] R. B. Wiringa, V. Fiks, and A. Fabrocini, Phys. Rev. C **38**, 1010 (1988).
- [4] E. Epelbaum, H.-W. Hammer, and Ulf-G. Meißner, Rev. Mod. Phys. **81**, 1773 (2009).
- [5] R. Machleidt and D. R. Entem, Phys. Rep. **503**, 1 (2011).
- [6] H. -W. Hammer, A. Nogga, and A. Schwenk, Rev. Mod. Phys. **85**, 197 (2013).
- [7] N. Kalantar-Nayestanaki, E. Epelbaum, J. G. Messchendorp, and A. Nogga, Rep. Prog. Phys. **75**, 016301 (2012).
- [8] J. D. Holt, J. Menéndez, J. Simonis, and A. Schwenk, Phys. Rev. C **90**, 024312 (2014).
- [9] A. Ekström *et al.*, Phys. Rev. C **91**, 051301(R) (2015).
- [10] K. Hebeler, S. K. Bogner, R. J. Furnstahl, A. Nogga, and A. Schwenk, Phys. Rev. C **83**, 031301(R) (2011).
- [11] F. Sammarruca, B. Chen, L. Coraggio, N. Itaco, and R. Machleidt, Phys. Rev. C **86**, 054317 (2012).
- [12] M. Kohno, Phys. Rev. C **88**, 064005 (2013).
- [13] M. Kohno, Prog. Theor. Exp. Phys. **123D02** (2015).
- [14] T. Krüger, I. Tews, K. Hebeler, and A. Schwenk, Phys. Rev. C **88**, 025802 (2013).
- [15] C. Drischler, V. Somà, and A. Schwenk, Phys. Rev. C **89**, 025806 (2014).
- [16] T. Krüger, K. Hebeler, A. Schwenk, Phys. Lett. B **744**, 18 (2015).
- [17] N. Kaiser, Eur. Phys. J. A **48**, 135 (2012).
- [18] N. Kaiser and R. Milkus, Eur. Phys. J. A **52**, no. 1, 4 (2016).
- [19] K. Sekiguchi *et al.*, Phys. Rev. C **89**, 064007 (2014).
- [20] F. A. Brieva and J. R. Rook, Nucl. Phys. A **291**, 299 (1977); *ibid.* 291, 317 (1977); *ibid.* 297, 206 (1978).
- [21] K. Amos, P. J. Dortmans, H. V. von Geramb, S. Karataglidis, and J. Raynal, in *Advances in Nuclear Physics*, edited by J. W. Negele and E. Vogt (Plenum, New York, 2000) Vol. 25, p. 275.
- [22] T. Furumoto, Y. Sakuragi, and Y. Yamamoto, Phys. Rev. C **78**, 044610 (2008).
- [23] S. Rafi, M. Sharma, D. Pachouri, W. Haider, and Y. K. Gambhir, Phys. Rev. C **87**, 014003 (2013).
- [24] Y. Yamamoto, T. Furumoto, N. Yasutake, and Th. A. Rijken, Phys. Rev. C **88**, 022801 (2013).
- [25] M. Toyokawa, M. Yahiro, T. Matsumoto, K. Minomo, K. Ogata and M. Kohno, Phys. Rev. C **92**, 024618 (2015).
- [26] T. Furumoto, Y. Sakuragi, and Y. Yamamoto, Phys. Rev. C **80**, 044614 (2009).
- [27] M. Toyokawa, K. Minomo, M. Kohno and M. Yahiro, J. Phys. G **42**, 025104 (2015).
- [28] K. Minomo, M. Toyokawa, M. Kohno and M. Yahiro, Phys. Rev. C **90**, 051601(R) (2014).
- [29] K. Egashira, K. Minomo, M. Toyokawa, T. Matsumoto and M. Yahiro, Phys. Rev. C **89**, 064611 (2014).
- [30] M. Kohno, Phys. Rev. C **96**, 059903(E) (2017).
- [31] M. Toyokawa, T. Matsumoto, K. Minomo and M. Yahiro, Phys. Rev. C **91**, 064610 (2015).
- [32] J. W. Holt, N. Kaiser, G. A. Miller, and W. Weise, Phys. Rev. C **88**, 024614 (2013).
- [33] E. Epelbaum, W. Glöckle, and Ulf-G. Meißner, Nucl. Phys. A **747**, 362 (2005).
- [34] H. V. von Geramb, K. Amos, L. Berge, S. Bräutigam, H. Kohlhoff and A. Ingemarsson, Phys. Rev. C **44**, 73 (1991).
- [35] P. J. Dortmans and K. Amos, Phys. Rev. C **49**, 1309 (1994).
- [36] D. F. Measday, Phys. Rev. **142**, 584 (1966).
- [37] T. Izumoto, S. Krewald, and A. Faessler, Nucl. Phys. A **341**, 319 (1980).
- [38] M. Yahiro, K. Minomo, K. Ogata, and M. Kawai, Prog. Theor. Phys. **120**, 767 (2008).
- [39] Y. C. Tang, M. LeMere, and D. R. Thompson, Phys. Rep. **47**, 167 (1978).
- [40] K. Aoki and H. Horiuchi, Prog. Theor. Phys. **69**, 857 (1983), and references therein.
- [41] K. Hagino, T. Takehi, and N. Takigawa, Phys. Rev. C **74**, 037601 (2006).
- [42] K. Minomo, K. Ogata, M. Kohno, Y. R. Shimizu, and M. Yahiro, J. Phys. G **37**, 085011 (2010).
- [43] D. T. Khoa, W. von Oertzen, and H. G. Bohlen, Phys. Rev. C **49**, 1652 (1994).
- [44] D. T. Khoa, G. R. Satchler, and W. von Oertzen, Phys. Rev. C **56**, 954 (1997).
- [45] J. F. Berger, M. Girod, and D. Gogny, Comput. Phys. Commun. **63**, 365 (1991).
- [46] T. Sumi *et al.*, Phys. Rev. C **85**, 064613 (2012).
- [47] H. de Vries, C. W. de Jager, and C. de Vries, At. Data Nucl. Data Tables **36**, 495 (1987).
- [48] R. P. Singhal, M. W. S. Macauley, and P. K. A. De Witt Huberts, Nucl. Instrum. and Method **148**, 113 (1978).
- [49] G. Hauser, R. Löhken, H. Rebel, G. Schatz, G. W. Schweimer, and J. Specht, Nucl. Phys. A **128**, 81 (1969).
- [50] D. A. Goldberg, S. M. Smith, H. G. Pugh, P. G. Roos, and N. S. Wall, Phys. Rev. C **7**, 1938 (1973).
- [51] B. Bonin *et al.*, Nucl. Phys. A **445**, 381 (1985).
- [52] M. Uchida *et al.*, Phys. Rev. C **69**, 051301 (2004).
- [53] H. Rebel, R. Löhken, G. W. Schweimer, G. Schatz, and G. Hauser, Z. Phys **256**, 258 (1972).
- [54] J. Albiński *et al.*, Nucl. Phys. A **445**, 477 (1985).
- [55] H. L. Clark, Y.-W. Lui, and D. H. Youngblood, Nucl. Phys. A **589**, 416 (1995).
- [56] Y.-W. Lui, D. H. Youngblood, H. L. Clark, Y. Tokimoto, and B. John, Phys. Rev. C **73**, 014314 (2006).
- [57] B. K. Nayak *et al.*, Phys. Lett. B **637**, 43 (2006).
- [58] D. A. Goldberg, S. M. Smith, and G. F. Burdick, Phys. Rev. C **10**, 1362 (1974).
- [59] D. H. Youngblood, Y. -W. Lui, and H. L. Clark, Phys. Rev. C **55**, 2811 (1997).
- [60] R. C. Fuller, Phys. Rev. C **12**, 1561 (1975).
- [61] B. Bonin *et al.*, Nucl. Phys. A **445**, 381(1985).
- [62] A. Ingemarsson *et al.*, Nucl. Phys. A **676**, 3 (2000).
- [63] <http://www.nt.phys.kyushu-u.ac.jp>